ARTICLE

Corrected: Author Correction

https://doi.org/10.1038/s41586-018-0607-z

Rock fluidization during peak-ring formation of large impact structures

Ulrich Riller[1]*, Michael H. Poelchau[2], Auriol S. P. Rae[3], Felix M. Schulte[1], Gareth S. Collins[3], H. Jay Melosh[4], Richard A. F. Grieve[5], Joanna V. Morgan[3], Sean P. S. Gulick[6,7], Johanna Lofi[8], Abdoulaye Diaw[8], Naoma McCall[6,7], David A. Kring[9] & IODP–ICDP Expedition 364 Science Party[10]

Large meteorite impact structures on the terrestrial bodies of the Solar System contain pronounced topographic rings, which emerged from uplifted target (crustal) rocks within minutes of impact. To flow rapidly over large distances, these target rocks must have weakened drastically, but they subsequently regained sufficient strength to build and sustain topographic rings. The mechanisms of rock deformation that accomplish such extreme change in mechanical behaviour during cratering are largely unknown and have been debated for decades. Recent drilling of the approximately 200-km-diameter Chicxulub impact structure in Mexico has produced a record of brittle and viscous deformation within its peak-ring rocks. Here we show how catastrophic rock weakening upon impact is followed by an increase in rock strength that culminated in the formation of the peak ring during cratering. The observations point to quasi-continuous rock flow and hence acoustic fluidization as the dominant physical process controlling initial cratering, followed by increasingly localized faulting.

Large hypervelocity impact structures show a distinct size–morphology progression[1] (Fig. 1), which depends on the gravity and target rock type of the impacted body. In this regard, the study of internal topographic rings—so-called peak rings[2]—are of particular importance in understanding the formation of peak-ring impact structures (Fig. 1b) and multi-ring impact basins (Fig. 1c)[3]. As crater diameter increases beyond the maximum size of a bowl-shaped crater, the depth-to-diameter ratio of the crater decreases. On Earth, peak-ring crater formation (Fig. 2, Supplementary Information) takes place in minutes[1,4] and implies extreme deformation rates accompanying large displacements. Peak-ring craters can be a few hundred kilometres in diameter, yet merely a few kilometres deep, with the peak rings greatly elevated above crater floors. To explain this topographic characteristic, peak-ring crater formation requires drastic mechanical weakening of the target rocks. Weakening is thought to be caused by a decrease in the angle of internal friction and cohesion and results in large-scale fluid-like behaviour of target rock during part of the cratering process[4–7]. Towards the end of the cratering process, however, rock strength needs to be sufficiently high to form and sustain topographically elevated peak rings.

A number of mechanisms for target-rock weakening have been proposed. These include impact-induced fracturing and fragmentation of the target rocks[8–16], wholesale thermal softening by shock heating[6], fault weakening[17] by shear heating[18] or other processes, and acoustic fluidization[19,20]. In this last process, short-wavelength, high-frequency pressure oscillations around the lithostatic pressure temporarily reduce the overburden pressure and, thus, friction between fractured target rocks.

Because direct observations are extremely limited, the exact mechanisms and duration of target rock weakening during large impact cratering are unknown. In particular, unequivocal physical evidence for acoustic fluidization or fault weakening in large impact craters remains to be identified. Large extra-terrestrial craters can only be analysed by remote sensing, which provides little or no subsurface structural information. With estimated original diameters between 200 km and 250 km, Vredefort (South Africa), Sudbury (Canada) and Chicxulub (Mexico), known as 'the big three'[21], are the largest impact structures known on Earth. Vredefort and Sudbury, however, are eroded to variable depths[22] of about 10 km and about 5 km, respectively, and so are largely missing the upper and most displaced target rocks (Fig. 2d). Chicxulub is the sole near-pristine, large impact structure with a topographic peak ring on Earth (Fig. 1d)[23–27], but post-impact sedimentary strata hundreds of metres thick have buried the impact structure, hindering direct access to the target rocks. Recent drilling by Expedition 364 of the International Ocean Discovery Program (IODP) with the International Continental Scientific Drilling Program (ICDP)[24,28] into the target rocks that constitute the peak ring at Chicxulub has now provided unprecedented insight into target rock deformation, weakening mechanisms and peak-ring formation in large-scale impact cratering.

Structural characteristics of target rock

A total of 829 m of core was recovered from Expedition 364 borehole M0077A (Fig. 1d), starting at 506 m below sea floor (m.b.s.f.)[24,28]. The recovered core includes 112 m of post-impact pelagic carbonate rock, followed by 130 m of impact melt rock and suevite, and 587 m of pervasively shocked target rock. The target rock consists of coarse-grained, alkali-feldspar-rich granitoid rock hosting uniformly oriented, pre-impact mafic and felsic sheet intrusions (Extended Data Fig. 1). At depths between 1,220 and 1,316 m.b.s.f., the target rock is mingled with impact melt rock on the decimetre to metre scale. Elsewhere in the target rock, impact melt rock is rather sparse. The mean density (2.41 g cm^{-3}) and mean P-wave velocity (4.1 km s^{-1}) of the target rock are considerably lower than those of typical felsic basement rocks (>2.6 g cm^{-3} and >5.5 km s^{-1})[24,28]. These petrophysical characteristics indicate substantial mechanical modification of the rock, notably in terms of increased porosity[29].

[1]Institut für Geologie, Universität Hamburg, Hamburg, Germany. [2]Department of Geology, Universität Freiburg, Freiburg, Germany. [3]Department of Earth Science and Engineering, Imperial College London, London, UK. [4]Department of Earth, Atmospheric and Planetary Sciences, Purdue University, West Lafayette, IN, USA. [5]Centre for Planetary Science and Exploration, Western University, London, Ontario, Canada. [6]Institute for Geophysics, University of Texas, Austin, TX, USA. [7]Department of Geological Sciences, Jackson School of Geosciences, University of Texas, Austin, TX, USA. [8]Géosciences Montpellier, CNRS, Université de Montpellier, Montpellier, France. [9]Universities Space Research Association, Lunar and Planetary Institute, Houston, TX, USA. [10]A list of participants and their affiliations appears at the end of the paper. *e-mail: ulrich.riller@uni-hamburg.de

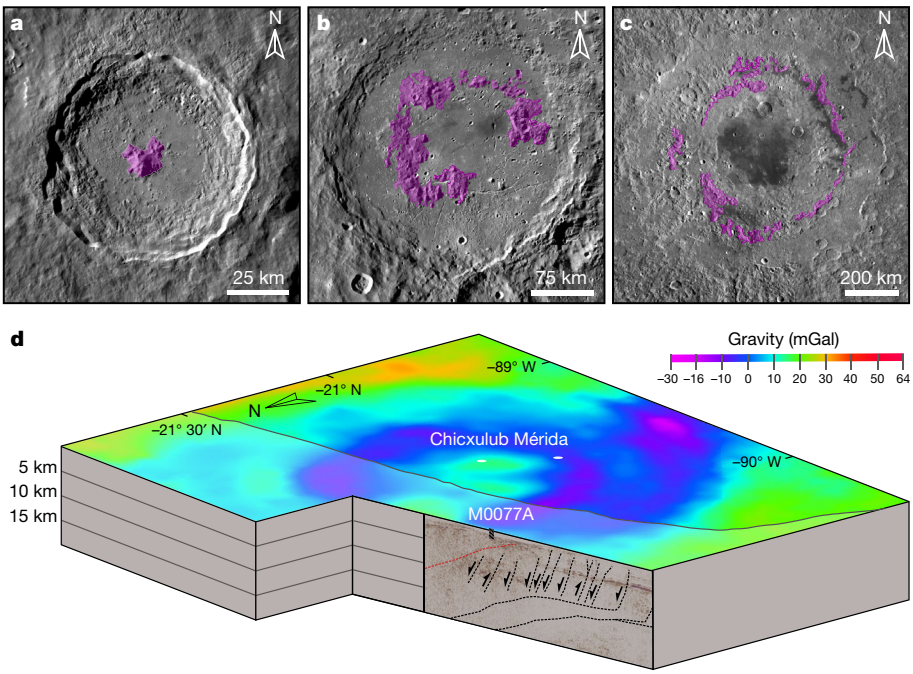

Fig. 1 | Typical impact structures on the Moon (http://quickmap.lroc.asu.edu) and the geophysical characteristics of the Chicxulub impact structure. Topographically elevated areas in **a**–**c** are highlighted in magenta. **a**, Tycho (diameter 85 km) is a central-peak crater. **b**, Schrödinger[34] (diameter 312 km) is a peak-ring impact structure. **c**, Orientale (diameter 930 km) is a multi-ring impact basin. **d**, Combined Bouguer gravity and seismic line A[27] of the Chicxulub impact structure. Offshore seismic data[27] indicate that the Chicxulub peak ring roughly correlates with a gravity low. The location of drill hole M0077A on the peak ring is indicated. Half-arrows indicate the sense of displacement on faults.

The post-impact carbonate rock is unstrained. Pre-impact deformation, however, of the granitoid target rock is evident through the sporadic presence of weak shape-preferred orientations of alkali-feldspar, plagioclase, quartz and biotite. The grain-shape alignment of these minerals formed under high-grade metamorphic conditions, as indicated by viscous deformation of feldspars and quartz[28]. Crystal-plastic strain cannot account for the reduced density and P-wave velocity of the target rock. Consequently, impact processes, including the damage caused by the passage of the shock wave, and deformation during peak-ring formation, must have caused the anomalous geophysical properties of the target rock[29].

Observed shock-induced structures in the target rock consist of shatter cones, microscopic planar deformation features and planar fractures in quartz and feldspars, as well as kinked biotite[28]. Severe structural target rock modification is evident by brittle and viscous deformation structures, including: (1) pervasive, irregular grain-scale fractures, (2) zones of cataclasite and ultra-cataclasite, (3) striated shear faults, (4) crenulated mineral foliations, and (5) brittle–ductile band structures (Figs. 3 and 4). The formation of (1) to (3) substantially increases the volume of deformed rock and thus accounts for the observed reduction in density and P-wave velocity[29].

The spatial distribution of macroscopic deformation structures indicates highly heterogeneous deformation in the target rock (Fig. 3). Microscopic inspection of the granitoid target rock reveals the pervasive presence of intra- and inter-granular dilation fractures displaying jigsaw fragment geometry (Fig. 4a). Zones of strongly comminuted material separate displaced mineral fragments (Fig. 4b). These cataclasite zones range in thickness from millimetres to centimetres (Fig. 4a–c, g) and indicate local differential shearing during cataclastic deformation. Locally, cataclasite zones grade into, or are truncated by, flow-foliated ultra-cataclasite, characterized by alternating quartz- and feldspar-rich layers (Fig. 4d). Crystal-plastic distortion of plagioclase (Fig. 4e) and quartz (Fig. 4f) indicate that the target rock accumulated some plastic strain before pervasive fracturing and cataclastic flow. Zones of (ultra-)cataclasite and crude mineral foliations, defined by the shape-preferred orientation of biotite and coarse layers of quartz and feldspars, are sporadically kinked (Fig. 4g, h). In summary, cataclastic deformation displays variable intensity throughout the cored target rock, which is evident by its localization and variable degree of comminution.

A total of 602 shear faults, with well-defined slip lineations, were recorded in the granitoid target rock (Fig. 3), with the total number of shear faults being vastly higher. By contrast, only 13 shear faults with slip lineations were identified in the post-impact carbonate rock and consist of a few millimetre-long calcite fibres (Fig. 4i), typical of seismic stick–slip faulting[30]. Slip lineations in the target rock, however, form pronounced ridges and grooves of strongly comminuted host rock material (Fig. 4j). Displacements on these faults may amount to several decimetres[28]. Although the post-impact carbonate rock shows a weak tectonic overprint, it is evident that the granitoid target rocks underwent catastrophic and pervasive shear faulting.

At 1,220 to 1,316 m.b.s.f., the target rock is strongly distorted and brecciated, and fragments of it are marginally resorbed and found in melt rock (Fig. 5a, b). Conversely, zones of brecciated target rock host elongated, and frequently wispy, melt-rock fragments, reminiscent of suevite (Fig. 5c, d). Where in contact with target rock fragments, the melt rock underwent large ductile strains, as is clear from the highly stretched granitoid fragments contained in the melt rock (Fig. 5e). Overall, the melt rock is spatially associated with the highest-strained target rocks, indicated by breccia of thicknesses of decimetres to metres. The presence of exotic fragments (Fig. 5f)—consisting of gneiss, mafic igneous rock and various mylonites—in the melt rock excludes an in situ frictional melt origin for the melt rock. Breccia zones are substantially thicker and show a larger range in sizes and shapes of fragments than cataclasite and ultra-cataclasite zones in target rock outside this particular depth interval. The differences in thickness and fragment size between these breccia and the cataclasite zones indicate different fragmentation mechanisms and/or fragmentation at different times during the cratering process. Finally, the spatial density of ductile band structures is maximal within

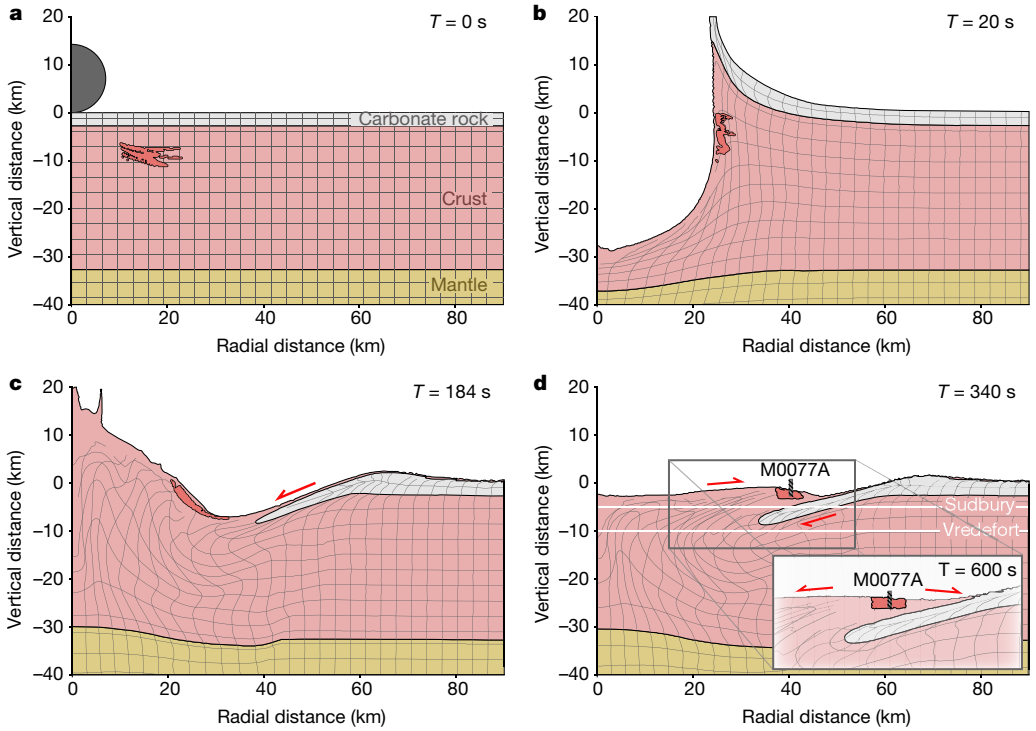

Fig. 2 | Modelled formation of the Chicxulub impact structure. The mechanism is based on numerical modelling of peak-ring crater formation[4,23,24,34]. A grid of tracer particles is shown to highlight the sub-crater deformation. Dark red area of crust in each panel tracks the material that eventually forms the peak ring. *T* denotes time in seconds after impact. Red half-arrows indicate the direction of major shear displacements relative to adjacent material. **a**, Undisturbed configuration of model lithosphere before impact. **b**, Cratering starts by shock-wave-induced, crustal-scale excavation of a bowl-shaped transient cavity. **c**, Gravitational instability of the transient cavity causes uplift of the crater centre and concomitant inward slumping of the cavity wall. **d**, Collapse and radial outward displacement of uplifted material over inward-slumped cavity wall segments followed by gravitational settling of the peak ring (inset) characterize the terminal phase of modelled crater modification. White lines indicate the approximate current erosion levels of the Sudbury and Vredefort impact structures.

this depth interval (Fig. 3). Brittle–ductile band structures occur predominantly in mechanically and thermally weakened target and melt rock and form ductile shear zones (Fig. 5f), shear bands with C–S fabric geometry (Fig. 5g)[31] and crenulated mineral fabrics (Fig. 4h).

Chronology of deformation mechanisms

Most importantly, it is possible to determine the relative timing of the various deformation mechanisms. Zones of (ultra-)cataclasite truncate the jigsaw fragment geometry of pervasively fractured target rock (Fig. 4a, b). Shear faults, in turn, consistently offset cataclasite and ultra-cataclasite zones (Figs. 4c and 5a, b). Target rock fragments in melt rock are sporadically striated and host cataclasite zones[28]; whereas melt rock matrices are devoid of shear faults. Cataclasite and melt rock are found in tension fractures (Fig. 5h), which, to some extent, formed from shear faults. Brittle–ductile band structures displace zones of cataclasite, crenulated foliation surfaces and the contacts of target rock with cataclasite and melt rock (Figs. 4g, h and 5f, g). In summary, pervasive fracturing of target rock was followed, respectively, by formation of (ultra-)cataclasite zones, shear faulting, emplacement of cataclasite and impact melt into dilatant fractures and formation of ductile band structures.

Deformation mechanisms and cratering stages

During the various cratering stages, deformation kinematics and states of stress of the target rock differ profoundly (Fig. 2). Therefore, distinct deformation mechanisms recognized in the target rock may well relate to individual cratering stages denoted in terms of time after impact. Shock and decompression causes irreversible plastic deformation and imparts to the shocked rocks a divergent outward velocity field, which forms the transient cavity. This velocity field causes wall-parallel extension and perpendicular shortening of the target rock (Fig. 2b). Rock deformation at upper-crustal pressures and depths, which is where peak-ring materials are derived from, is accommodated by fracturing. We therefore attribute pervasive fracturing, which preceded the other deformation mechanisms, to shock loading, decompression and transient cavity growth (time after impact $T < 30$ s).

After the transient cavity forms (Fig. 2b), gravitational collapse modifies the crater shape until the final crater morphology is reached (Supplementary Information). During initial collapse, the peak-ring material motion transitions from outward and divergent excavation flow to inward and convergent rock flow towards the crater centre. This inward movement leads to the incorporation of peak-ring material onto the flank of a central uplift (Fig. 2c). During this stage of cratering, peak-ring materials experience several distinct stress states (Extended Data Fig. 2). Planar zones of cataclasite and (ultra-)cataclasite are plausible candidates for accommodating the deformation of pre-fractured target rock during this cratering stage ($20\ \text{s} < T < 150$ s).

During build-up of the central uplift ($20\ \text{s} < T < 100$ s), the pressure on the peak-ring material increases (Extended Data Fig. 2). This increase inevitably closes asperities within the fractured rock and thus increases the internal friction of the target rock and normal stresses on faults. The central uplift eventually over-heightens and becomes gravitationally unstable, causing downwards and radial-outward collapse ($160\ \text{s} < T < 300$ s). In this motion, collapsed material piles up to form the peak ring, which is thrust over the inwardly slumped transient cavity rim (Fig. 2d, Supplementary Information). Collectively, the increased pressure, combined with the reversal of the material displacement field as the central uplift transitions from motion upwards to outwards and downwards during collapse accounts for the observed transition from localized cataclastic flow to shear faulting during this stage of cratering.

As the melt rock occurrences within the target rock are devoid of shear faults, melt emplacement must occur at the end of peak-ring

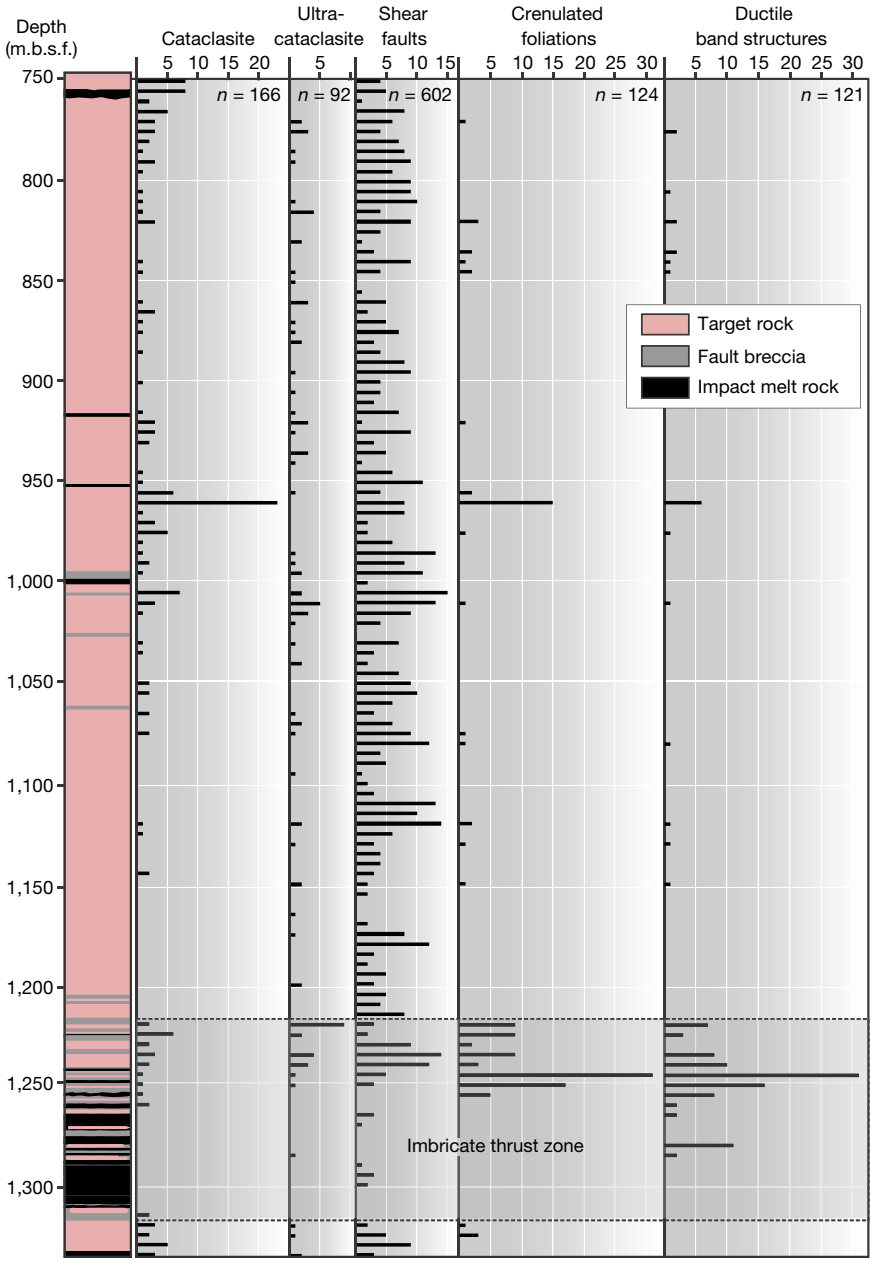

Fig. 3 | Spatial distribution of major lithological units and deformation structures in target rock of M0077A drill core. *n* is number of observations. We note the strong spatial correlation of increased numbers of (ultra-)cataclasite zones, crenulated foliations and ductile band structures below 1,220 m.b.s.f.

formation (250 s < T < 600 s). Subsequent deformation is evident from the ductile band structures displacing contacts between the target and melt rock, zones of cataclasite and mineral foliations. Band orientation, the sense of displaced layers and fabric asymmetry, as displayed by sigmoidal foliation planes and cataclasite zone boundaries, consistently indicate band formation through normal faults (Figs. 4g, h and 5f, g). Respective vertical shortening and horizontal extension is consistent with gravitational spreading of the topographically elevated peak ring and signifies the final stage of crater modification (inset in Fig. 2d).

Weakening mechanisms

The recognition of distinct deformation mechanisms corresponding to the various stages of the cratering process is of fundamental importance in comprehending the mechanics of large-scale impact cratering. Initial pervasive grain-scale fracturing causes a profound loss of cohesion in target rocks at the onset of, and during, transient cavity growth. During cavity modification, strain is localized progressively through formation of cataclasite zones, ultra-cataclasite zones, shear faults, and finally deformation on fault zones with impact-melt-bearing fault breccias. Progressive strain localization is evidence of the incremental regaining of shear and cohesive strength in the target rock, as crater modification proceeds. It has been proposed that crater collapse is facilitated by the self-lubrication of faults by frictional melts[18]. We did not, however, uncover any evidence for friction-generated melt rock in the recovered target rock from the peak ring at Chicxulub. Hence, dynamic weakening of faults, if important, appears to require a mechanism other than shear heating.

Shock compression and dilation during initial impact caused wholesale intra-crystalline damage (Fig. 4e, f). Thereafter, dynamic fracturing induced by the passage of the shock and rarefaction waves and transient cavity growth led to loss in cohesion and shear strength. The presence of pervasively fractured target rock with preserved microscopic jigsaw fragment patterns and uniform orientation of pre-impact dykes (Extended Data Fig. 1) indicate that target rock above 1,220 m.b.s.f.

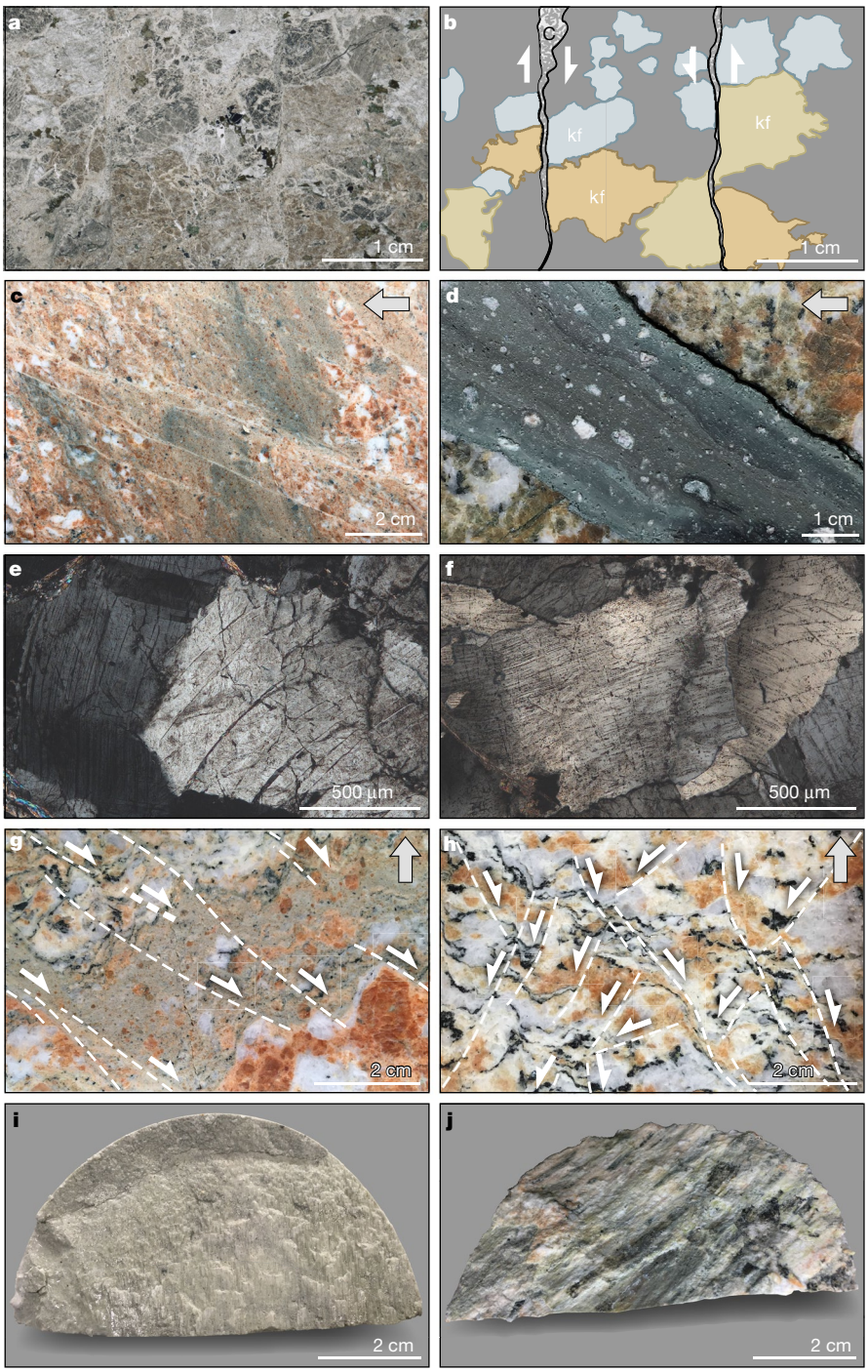

Fig. 4 | Deformation structures in target rock at site M0077A. Arrow indicates the direction of the top of the drill core. Half-arrows indicate the sense of displacement on discontinuities. **a**, Photomicrograph in plane-polarized light showing pervasive cataclasite of granitoid target rock (core 122-3, 820 m.b.s.f.). **b**, Line drawing of **a** showing alkali-feldspar (kf) displaced on cataclasite zone (**c**). **c**, Cataclasite zones displaced on shear faults (core 301-1, 1,326.45–1,326.57 m.b.s.f.). **d**, Flow-foliated ultra-cataclasite (core 215-2, 1,065.85–1,065.94 m.b.s.f.). **e**, Photomicrograph in cross-polarized light showing distorted twin lamellae in plagioclase (core 129-1, 831.38–831.40 m.b.s.f.). **f**, Photomicrograph in cross-polarized light showing distorted quartz with planar deformation features (core 129-1, 831.38–831.40 m.b.s.f.). **g**, Cataclasite zone segmented by normal faults (core 172-2, 956.41–956.45 m.b.s.f.). **h**, Crenulated layering in granitoid rock (core 122-1, 817.61–817.66 m.b.s.f.). **i**, Striated shear fault in carbonate rock. **j**, Striated shear fault in granitoid target rock (core 154-1, 894.19 m.b.s.f.).

behaved largely as a structurally coherent rock mass. The implication of small displacements across the entire rock mass is consistent with macroscopic deformation of an acoustically fluidized rock mass[19,20].

Structural observations from the peak-ring target rocks of Chicxulub are generally consistent with acoustic fluidization as the dominant weakening mechanism and offer insight for the refinement of future impact simulations. Acoustic fluidization entails target rock blocks undergoing pressure oscillations around the ambient lithostatic stress[4,7,19,20]. During pressure lows, blocks have reduced normal stresses between them, drastically reducing frictional resistance at block boundaries during periodic rock flow. During pressure highs, blocks are compressed, locally increasing the frictional resistance of the deforming rock mass. Cataclasite zones seem likely to be where the sheared block boundaries serve as contact strain zones during oscillation of target

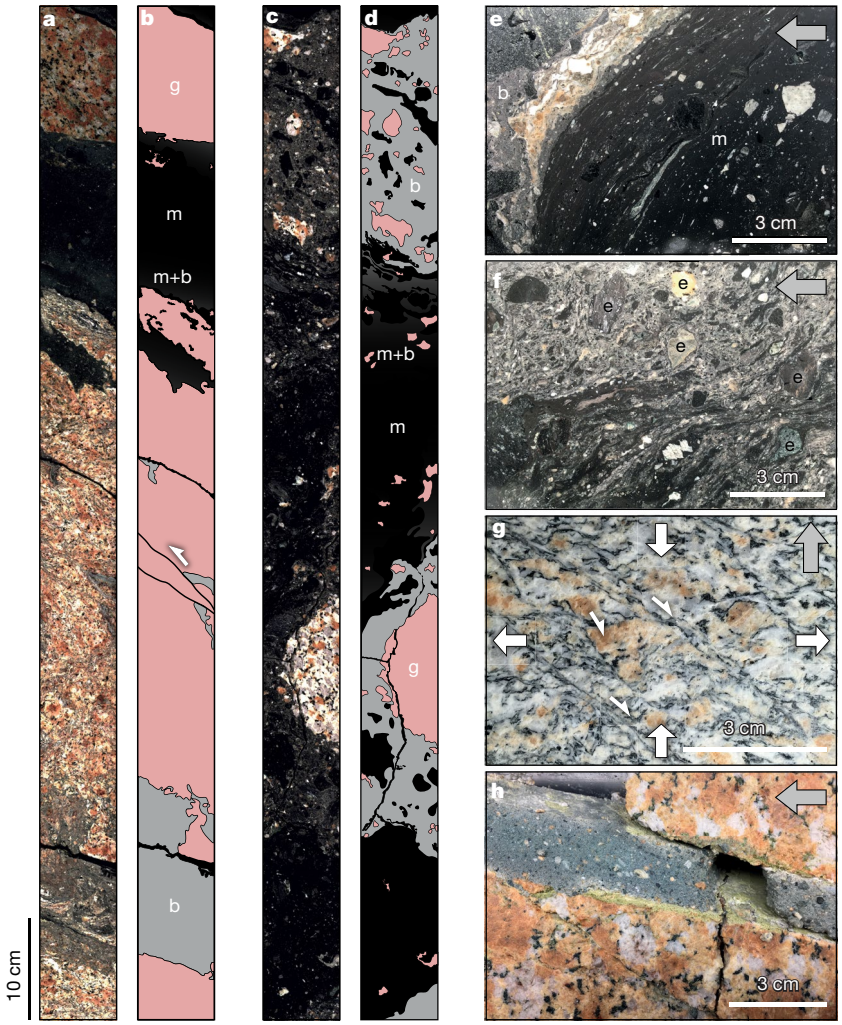

Fig. 5 | Images illustrating rock types found between 1,220 and 1,316 m.b.s.f. (g, highly distorted granitoid rock; m, impact melt rock; b, fault breccia; e, exotic fragments.) **a**, Line scan of core 265-2 (1,216.36–1,217.45 m.b.s.f.), showing highly distorted and brecciated target rock mingled within melt rock. We note halos of mingled melt rock and fault breccia at the margins of granitoid rocks as well as shear faults (half-arrow) displacing thin zones of ultra-cataclasite. **b**, Line drawing of **a**. **c**, Line scan of core 285-1 (1,277.24–1,278.25 m.b.s.f.), displaying mingling of impact melt rock and fault breccia, notably near the granitoid fragment. We note melt rock fragments within fault breccia. **d**, Line drawing of **c**. **e**, Melt rock in contact with fault breccia. We note the gradient in contact strain, evident from the stretched target rock fragments in melt rock (core 303-3, 1,334.24–1,334.35 m.b.s.f.). **f**, Ductile shear zone in mingled impact melt rock and fault breccia containing exotic fragments (core 289-1, 1,289.75–1,289.87 m.b.s.f.). **g**, C–S fabric geometry in granitoid indicated by displaced planar mineral fabric in granitoid target rock (half arrows) amounting to vertical shortening and horizontal extension (white arrows) (core 273-2, 1,241.26–1,241.31 m.b.s.f.). **h**, Cataclasite entrained in dilatant fracture (core 262-1, 1,207.45–1,207.56 m.b.s.f.).

rock blocks. Continued cataclasis, resulting in flow-foliated ultra-cataclasite, heralds an increase in shear strain of the rock mass and waning acoustic fluidization. While in motion, continued comminution in (ultra-)cataclasite zones may generate additional acoustic energy and prolong cataclastic flow[20].

A critical parameter in the acoustic fluidization model is the dominant wavelength of pressure vibrations[19], which controls both the viscosity of the acoustically fluidized rock mass and the timescale for the decay of vibrations. The 'block model' of acoustic fluidization is employed in most Chicxulub-scale impact simulations[4,23,24], such as the one reproduced in Fig. 2. The block model supposes that the subcrater rock mass is dominated by blocks of a characteristic size that oscillate within a surrounding mass of breccia with a single vibrational wavelength (and period) that is directly proportional to the block size[32]. The block model parameters employed in Chicxulub impact simulations imply a block size of about 100–500 m (depending on the assumed acoustic energy dissipation factor Q) and an oscillation frequency of a few hertz. This prediction is consistent with the entire approximately 450-m granite sequence above the imbricate thrust zone representing a single 'block' (Fig. 3).

On the other hand, if the cataclasite zones observed in the Chicxulub peak-ring drill core represent oscillating-block boundaries as we propose, their average spacing (Fig. 3) of about 3.5 m (2.3 m including ultra-cataclasite zones) would imply a much smaller block size, shorter dominant vibrational wavelength and higher vibrational frequency[19,20]. This would imply rapid evolution of the acoustic wave field during collapse of the crater, which is not predicted by the current block model implementation. High-frequency vibrations sustained for the duration of crater collapse, however, could be explained by the efficient regeneration of acoustic energy during the cratering process, which is neglected in the block model. Effective regeneration of vibrations in a rapidly shearing rock mass is consistent with findings from discrete-element models of acoustic fluidization in landslides[33]. Alternatively, the acoustic wave field may evolve by progressive lengthening of the dominant vibrational wavelength during cratering as higher-frequency vibrations dissipate sooner. In this case, the effective block size could increase during crater formation from a few metres at the beginning of modification, when the first cataclasite zones are likely to have formed ($20\ \mathrm{s} < T < 60\ \mathrm{s}$), to a few hundred metres by the end of peak-ring emplacement ($T < 600\ \mathrm{s}$).

A progressive waning of the acoustic wavefield in which slip events, facilitated by negative pressure excursions, become less frequent and more widely spaced is consistent with the temporal evolution of deformation observed in the drill core. This evolution suggests a progression from distributed, small-displacement deformation along closely spaced faults early in the cratering process to more localized, larger-displacement deformation along widely spaced slip surfaces later. Acoustic fluidization is, therefore, interpreted to halt at the onset of shear faulting, as target rock blocks cease to oscillate and the bulk rock mass regains internal friction and, thus, shear strength. Whether this cessation of acoustic fluidization occurs during the final emplacement of the peak ring (as suggested by current numerical simulations; Fig. 2d) or earlier, during the formation of the central uplift, is unclear. In the latter scenario, the outward collapse of the central uplift and thrusting of peak-ring rocks onto the transient cavity rim would have occurred after the rocks regained most of their large-scale static strength. In this case, the late stages of collapse could have been facilitated by large faults, lubricated by entrained impact melt.

Peak-ring formation

Modelling suggests that the target rock forming the peak ring resided at a depth[24] of about 10 km, before impact, and was entrained into a central uplift before being thrust outward over inward slumped transient cavity wall segments (Fig. 2). From the modelled cratering flow (Supplementary Information), it is conceivable that individual target rock blocks may over-thrust portions of impact melt, notably where the peak ring develops. Impact melt may then become sandwiched between quasi-coherent target rock masses. Hence, impact melt in large craters may be present not only as ponded liquids at the surface, but also as melt bodies or sheets entrained and trapped in target rock thrust zones at depth.

Structural and lithological characteristics of the rocks at depths between 1,220 and 1,316 m.b.s.f. are consistent with impact melt entrained in a prominent imbricate thrust zone (Fig. 3). Respective characteristics include: (1) the concentration of high strains in target rock and melt rock (Fig. 5a, e), (2) the strongly distorted target rock slivers mingled with melt rock and breccia, interpreted as fault breccia (Fig. 5a–d, f), (3) the occurrence of melt rock fragments in fault breccia (Fig. 5c, d, f), and (4) fragment lithologies not present in the adjacent target rock[28]. Given that in situ frictional melting is excluded for the origin of the melt rock, formation of this rock by shock-induced melting and subsequent entrainment during peak-ring formation appears to be the more plausible explanation. Specifically, we propose that the target rock mass above 1,220 m.b.s.f. over-thrust and buried the impact melt overlying the deeper target rock, which is now found below 1,316 m.b.s.f. Impact melt rock in contact with brecciated target rock displays large ductile strains (Fig. 5e) and indicates rapid cooling (quenching) and solidification of the impact melt during thrusting. In summary, imbricate thrusting (stacking) of target rock masses[34] contributed to the high topography of the peak ring. A prerequisite for thrusting is the regaining of shear strength in the target rock by the time of the formation of peak-ring topography.

Consequences of dynamic weakening

Examination of the deformation mechanisms of the target rocks underlying the peak ring at Chicxulub has provided unprecedented evidence for the physical mechanisms responsible for weakening and the regained strength of target rock during large-scale impact cratering. Results are strongly supportive of the dynamic collapse model (Fig. 2, Supplementary Information) of peak-ring formation and of acoustic fluidization as the dominant mechanism driving crater modification. The transition in deformation style from distributed cataclastic flow to localized shear-faulting and the progressive increase in fault spacing illuminates the waning of acoustic fluidization and the target regaining sufficient strength to support the topography of the peak ring. Dynamic weakening of faults or regeneration of acoustic energy may have an important role in this final phase of peak-ring formation. Incorporating this insight into future numerical impact simulations will aid in the design of higher-fidelity models of large-scale impact cratering.

In particular, we regard (ultra-)cataclasite zones, serving as contact strain zones of oscillating target rock blocks, as the physical manifestation of pressure fluctuations. If so, the estimated average size of coherent target rock blocks within the Chicxulub peak ring is one to two orders of magnitudes smaller than observed in the central uplifts of smaller terrestrial complex craters[35–37]. This may imply efficient regeneration of pressure fluctuations during transient cavity collapse and modification or a growth in vibrational wavelength as the wavefield evolves. In either case, central peaks of smaller impact structures may be preserved because fluidization ceased early in the gravitational collapse process. By contrast, peak rings in peak-ring craters and multi-ring basins form because acoustic fluidization is sustained through the formation and collapse of an overheightened central uplift.

Online content

Any methods, additional references, Nature Research reporting summaries, source data, statements of data availability and associated accession codes are available at https://doi.org/10.1038/s41586-018-0607-z.

Received: 28 February 2018; Accepted: 15 August 2018;
Published online 24 October 2018.

1. Croft, S. K. The modification stage of basin formation: conditions of ring formation. *Geochim. Cosmochim. Acta* **12A**, 227–257 (1981).
2. Grieve, R. A. F., Robertson, P. B. & Dence, M. R. Constraints on the formation of ring impact structures, based on terrestrial data. *Geochim. Cosmochim. Acta* **12A**, 37–57 (1981).
3. Neumann, G. A. et al. Lunar impact basins revealed by gravity recovery and interior laboratory measurements. *Sci. Adv.* **1**, e1500852 (2015).
4. Ivanov, B. A. Numerical modelling of the largest terrestrial meteorite craters. *Sol. Syst. Res.* **39**, 381–409 (2005).
5. Melosh, H. J. & Ivanov, B. A. Impact crater collapse. *Annu. Rev. Earth Planet. Sci.* **27**, 385–415 (1999).
6. O'Keefe, J. D. & Ahrens, T. J. Planetary cratering mechanics. *J. Geophys. Res.* **98**, 17011–17028 (1993).
7. Wünnemann, K. & Ivanov, B. A. Numerical modelling of the impact crater depth-diameter dependence in an acoustically fluidized target. *Planet. Space Sci.* **51**, 831–845 (2003).
8. Grady, D. E. & Kipp, M. E. in *Fracture Mechanics of Rock* (ed. Atkinson, B. K.) 429–475 (Academic Press, London, 1987).
9. Fujiwara, A., Kamimoto, G. & Tsukamoto, A. Destruction of basaltic bodies by high-velocity impact. *Icarus* **31**, 277–288 (1977).
10. Ahrens, T. J. & Rubin, A. M. Impact-induced tensional failure in rock. *J. Geophys. Res.* **98**, 1185–1203 (1993).
11. Buhl, E. et al. Particle size distribution and strain rate attenuation in hypervelocity impact and shock recovery experiments. *J. Struct. Geol.* **56**, 20–33 (2013).
12. Collins, G. S. Numerical simulations of impact crater formation with dilatancy. *J. Geophys. Res.* **119**, 2600–2619 (2014).
13. Melosh, H. J., Ryan, E. V. & Asphaug, E. Dynamic fragmentation in impacts: hydrocode simulation of laboratory impacts. *J. Geophys. Res.* **97**, 14,735–14,759 (1992).
14. Kenkmann, T. Folding within seconds. *Geology* **30**, 231–234 (2002).
15. Kenkmann, T. Dike formation, cataclastic flow, and rock fluidization during impact cratering: an example from the Upheaval Dome structure, Utah. *Earth Planet. Sci. Lett.* **214**, 43–58 (2003).
16. Collins, G. S., Melosh, H. J. & Ivanov, B. A. Modeling damage and deformation in impact simulations. *Meteorit. Planet. Sci.* **39**, 217–231 (2004).
17. Senft, L. E. & Stewart, S. T. Dynamic fault weakening and the formation of large impact craters. *Earth Planet. Sci. Lett.* **287**, 471–482 (2009).
18. Spray, J. G. Superfaults. *Geology* **25**, 579–582 (1997).
19. Melosh, H. J. Acoustic fluidization: a new geological process? *J. Geophys. Res.* **84**, 7513–7520 (1979).
20. Melosh, H. J. Dynamical weakening of faults by acoustic fluidization. *Nature* **379**, 601–606 (1996).
21. Grieve, R. A. F. & Therriault, A. Vredefort, Sudbury, Chicxulub: three of a kind? *Annu. Rev. Earth Planet. Sci.* **28**, 305–338 (2000).
22. Grieve, R. A. F., Reimold, W. U., Morgan, J., Riller, U. & Pilkington, M. Observations and interpretations at Vredefort, Sudbury and Chicxulub: towards a composite kinematic model of terrestrial impact basin formation. *Meteorit. Planet. Sci.* **43**, 855–882 (2008).
23. Collins, G. S., Melosh, H. J., Morgan, J. V. & Warner, M. R. Hydrocode simulations of Chicxulub crater collapse and peak-ring formation. *Icarus* **157**, 24–33 (2002).
24. Morgan, J. V. et al. The formation of peak rings in large impact craters. *Science* **354**, 878–882 (2016).

25. Morgan, J. V., Warner, M. R., Collins, G. S., Melosh, H. J. & Christeson, G. L. Peak-ring formation in large impact craters: geophysical constraints from Chicxulub. *Earth Planet. Sci. Lett.* **183**, 347–354 (2000).
26. Morgan, J. V. et al. Full waveform tomographic images of the peak ring at the Chicxulub impact crater. *J. Geophys. Res.* **116**, B06303 (2011).
27. Gulick, S. P. S. et al. Importance of pre-impact crustal structure for the asymmetry of the Chicxulub impact crater. *Nat. Geosci.* **1**, 131–135 (2008).
28. Morgan, J. V. et al. Chicxulub: drilling the K-Pg impact crater. In *Proceedings of the International Ocean Discovery Program 364* https://doi.org/10.14379/iodp.proc.364.2017 (International Ocean Discovery Program, College Station, 2017).
29. Christeson, G. L. et al. Extraordinary rocks from the peak ring of the Chicxulub impact crater: P-wave velocity, density, and porosity measurements from IODP/ICDP Expedition 364. *Earth Planet. Sci. Lett.* **495**, 1–11 (2018).
30. Petit, J. P. Criteria for the sense of movement on fault surfaces in brittle rocks. *J. Struct. Geol.* **9**, 597–608 (1987).
31. Berthé, D., Choukroune, P. & Jegouzo, P. Orthogneiss, mylonite and non-coaxial deformation of granites: the example of the South Armorican Shear Zone. *J. Struct. Geol.* **1**, 31–42 (1979).
32. Ivanov, B. A. & Artemieva, N. A. in *Catastrophic Events and Mass Extinctions: Impact and Beyond* (eds C. Koeberl, C. & MacLeod, K. G.) Geological Society of America Special Paper **356**, 619–630 (GSA, 2002).
33. Johnson, B. C., Campbell, C. S. & Melosh, H. J. The reduction of friction in long runout landslides as an emergent phenomenon. *J. Geophys. Res.* **121**, 881–889 (2016).
34. Kring, D. A., Kramer, G. Y., Collins, G. S., Potter, R. W. K. & Chandnani, M. Peak-ring structure and kinematics from a multi-disciplinary study of the Schrödinger impact basin. *Nat. Commun.* **7**, 13161 (2016).
35. Ivanov, B. A., Kocharyan, G. G. & Kostuchenko, V. N. Puchezh-Katunki impact crater: preliminary data on recovered core block structure. In *Proc. 27th Lunar and Planetary Science Conf.* 589–590, https://www.lpi.usra.edu/meetings/lpsc1996/pdf/1295.pdf (1996).
36. Kenkmann, T., Collins, G. S. & Wünnemann, K. in *Impact Cratering: Processes and Products* (eds Osinski, G. R. & Pierazzo, E.) 60–75 (John Wiley & Sons, Chichester, 2013).
37. Rae, A. S. P., Collins, G. S., Grieve, R. A. F., Osinski, G. R. & Morgan, J. V. Complex crater formation: insights from combining observations of shock pressure distribution with numerical models at the West Clearwater Lake impact structure. *Meteorit. Planet. Sci.* **52**, 1330–1350 (2017).

Acknowledgements This work was supported by the Priority Programs 527 and 1006 of the German Science Foundation (grants Ri 916/16-1 and PO 1815/2-1), National Science Foundation grants (OCE-1737351, OCE-1450528 and OCE-1736826), and Natural Environment Research Council (grants NE/P011195/1 and NE/P005217/1). The Chicxulub drilling expedition was funded by the European Consortium for Ocean Research Drilling (ECORD) and the IODP as Expedition 364 with co-funding from the ICDP. The Yucatan State Government and Universidad Nacional Autónoma de México (UNAM) provided logistical support. This research used samples and data provided by IODP. Samples can be requested at http://web.iodp.tamu.edu/sdrm. We are grateful for assistance from the staff of the IODP Core Repository in Bremen, Germany, during the Onshore Science Party. We thank B. Ivanov and C. Koeberl for constructive reviews and S. Teuber for assistance in figure preparation. This is UTIG contribution number 3,278.

Reviewer information *Nature* thanks B. Ivanov and C. Koeberl for their contribution to the peer review of this work.

Author contributions U.R., M.H.P., A.S.P.R., J.V.M., S.P.S.G. and R.A.F.G. conceived the study. All authors participated in sampling and data collection offshore and/or onshore during IODP-ICDP Expedition 364, interpretation of the data as well as writing and/or editing of the manuscript. U.R. provided the first draft of the manuscript. U.R. and F.M.S. acquired structural data from line scans. J.L. and A.D. provided the downhole orientation data. A.S.P.R and G.S.C. performed and analysed the numerical models; G.S.C., A.S.P.R. and H.J.M. contributed the discussion on the implications for acoustic fluidization.

Competing interests The authors declare no competing interests.

Additional information
Extended data is available for this paper at https://doi.org/10.1038/s41586-018-0607-z.
Supplementary information is available for this paper at https://doi.org/10.1038/s41586-018-0607-z.
Reprints and permissions information is available at http://www.nature.com/reprints.
Correspondence and requests for materials should be addressed to U.R.
Publisher's note: Springer Nature remains neutral with regard to jurisdictional claims in published maps and institutional affiliations.

IODP–ICDP Expedition 364 Science Party
Joanna V. Morgan[3], Sean P. S. Gulick[6,7], Sophie L. Green[11], Johanna Lofi[8], Elise Chenot[12], Gail L. Christeson[6], Philippe Claeys[13], Charles S. Cockell[14], Marco J. L. Coolen[15], Ludovic Ferrière[16], Catalina Gebhardt[17], Kazuhisa Goto[18], Heather Jones[19], David A. Kring[9], Long Xiao[20], Christopher M. Lowery[6,7], Rubén Ocampo-Torres[21], Ligia Perez-Cruz[22], Annemarie E. Pickersgill[23,24], Michael H. Poelchau[25], Auriol S. P. Rae[26], Cornelia Rasmussen[6,7], Mario Rebolledo-Vieyra[27], Ulrich Riller[1], Honami Sato[28], Jan Smit[29], Sonia M. Tikoo-Schantz[30], Naotaka Tomioka[31], Michael T. Whalen[32], Axel Wittmann[33], Kosei E. Yamaguchi[34,35], Jaime Urrutia Fucugauchi[22] & Timothy J. Bralower[19]

[11]British Geological Survey, The Lyell Centre, Research Avenue South, Edinburgh, UK. [12]Université de Bourgogne-CNRS, Biogeosciences Laboratory, Dijon, France. [13]Analytical, Environmental and Geochemistry (AMGC), Vrije Universiteit Brussel (VUB), Brussels, Belgium. [14]School of Physics and Astronomy, UK Center for Astrobiology, University of Edinburgh, Edinburgh, UK. [15]Western Australia Organic and Isotope Geochemistry Centre, School of Earth and Planetary Sciences, Curtin University, Bentley, Western Australia, Australia. [16]Natural History Museum, Vienna, Austria. [17]Alfred Wegener Institute Helmholtz Centre of Polar and Marine Research, Bremerhaven, Germany. [18]International Research Institute of Disaster Science, Tohoku University, Sendai, Japan. [19]Pennsylvania State University, University Park, PA, USA. [20]China University of Geosciences (Wuhan), School of Earth Sciences, Planetary Science Institute, Wuhan, China. [21]National Center of Scientific Research (CNRS), Groupe de Physico-Chimie de l'Atmosphère, Institut de Chimie et Procédés pour l'Energie, l'Environnement et la Santé ICPEES, Université de Strasbourg, Strasbourg, France. [22]Instituto de Geofísica, Universidad Nacional Autónoma De México, México City, Mexico. [23]School of Geographical and Earth Sciences, University of Glasgow, Glasgow, UK. [24]Argon Isotope Facility, Scottish Universities Environmental Research Centre (SUERC), East Kilbride, UK. [25]Department of Geology, University of Freiburg, Freiburg, Germany. [26]Department of Earth Science and Engineering, Imperial College London, London, UK. [27]Unidad de Ciencias del Agua, Mérida, Mexico. [28]Japan Agency for Marine-Earth Science and Technology, Yokosuka, Japan. [29]Faculty of Earth and Life Sciences, Amsterdam, The Netherlands. [30]Earth and Planetary Sciences, Rutgers University—New Brunswick, Piscataway, NJ, USA. [31]Japan Agency for Marine-Earth Science and Technology, Kochi Institute for Core Sample Research, Kochi, Japan. [32]Department of Geosciences, University of Alaska Fairbanks, Fairbanks, AK, USA. [33]Eyring Materials Center, Arizona State University, Tempe, AZ, USA. [34]Department of Chemistry, Toho University, Funabashi, Japan. [35]NASA Astrobiology Institute, Mountain View, CA, USA.

METHODS

Acquisition of structural data from drill core. In addition to the methods employed for visual appraisal as well as meso- and microstructural analyses of the drill core during the Onshore Science Party[38], the following analyses were conducted. On the basis of a detailed examination of drill core line-scans, the occurrence of cataclasite zones, ultra-cataclasite zones, crenulated foliations and ductile band structures was recorded with depth. Only zones of (ultra-)cataclasite displaying a thickness of 1 cm and larger were recorded. Distinction between the two types of cataclasite is based on grain size, the presence of flow foliation and the fragment-size distribution. Overall, ultra-cataclasite appears darker than cataclasite. Mesoscopic shear faults displaying slip lineations and slip sense were identified by carefully removing core sections from the liners. Statistical analysis of the spatial occurrence of the structures was conducted with Microsoft Excel (see Source Data for Fig. 3).

Microstructural analysis. Polished thin sections of thickness 25 μm were produced from selected target rock samples at the Institute of Mineralogy and Petrography of the University of Hamburg, Germany. Microscopic inspection of thin sections was conducted using a Zeiss Axio Scope.A1 polarization microscope and attached high-resolution digital camera AxioCam MRc Rev. 3 FireWire.

Borehole imaging of planar structures. During Expedition 364, both optical and acoustic borehole images of the borehole walls were acquired[38]. Post-acquisition processing and analysis allowed manual picking of the planar structural discontinuities, corresponding to pre-impact igneous sheet intrusions, and determination of their orientation. Orientations have not been corrected from borehole deviation, which departs less than 4° from the vertical. For visualization and processing of borehole images, the ALT WellCAD (https://www.alt.lu/products-wellcad/) software package was used. For analysis of orientation of pre-impact sheet intrusions the software package Tectonics FP version 1.6 was used[39].

Numerical modelling. To aid interpretation of the drill core data, we reproduced and reprocessed the numerical simulation of the Chicxulub impact[24], which was in turn based on previous Chicxulub impact simulations that produced a good match to geological and geophysical constraints[4,23,32,40]. The impactor parameters of the model were: diameter 14 km, velocity 12 km s^{-1}, density 2,630 kg m^{-3}. A vertical incidence impact angle was enforced by the cylindrical geometry of the two-dimensional model. A spatial resolution of 200 m was used, corresponding to 35 cells across the impactor radius. A simplified target structure was used of 3 km (carbonate) cover rocks and 30 km (granite) crust overlying (dunite) mantle. The simulation duration was 600 s of model time. We refer to ref. [24] for a full description of the modelling approach, including a comprehensive list of model parameters.

Simulations were processed to examine the motion and pressure of peak-ring materials (Fig. 2a–d, Extended Data Fig. 2, Supplementary Video). Lagrangian tracer particles employed in the numerical method allow the history of material that ends up within the peak ring to be recorded and interrogated. Ref. [24] used tracer particles to illustrate the peak pressure and provenance of the peak-ring materials, as well as its motion during crater formation. Here, we identified a subset of 100 tracer particles within the same peak-ring material, initially located within a square (2 km × 2 km) cross-section at a depth of 10 km and a radius of 16 km (see Supplementary Information, $T=0$). The Supplementary Video shows the motion of these tracers during cratering in both the fixed simulation reference frame (main image) and in a Lagrangian reference frame, centred on the average location of the 100 tracers (inset). The inset image gives a qualitative sense of the internal deformation of the peak-ring materials and highlights the deformation kinematics of peak-ring material during cratering.

Additionally, we analysed the pressure recorded by each tracer (circles) within the same volume, as well as the average pressure (solid line), as a function of time during the simulation (Extended Data Fig. 2). After the brief passage of the shock wave ($P>10$ GPa; $T<5$ s), the pressure in the peak-ring materials rises from 10–20 MPa to 50–100 MPa between about 100 s and about 250 s, before returning back to 10–20 MPa. Thus, the inward collapse of the peak-ring materials towards the central uplift and the subsequent outward collapse are associated with elevated pressures, above the ultimate overburden pressure in the peak-ring materials at their final location. We note that pressure waves caused by shockwave reflections from the numerical domain boundaries, which would not be present in reality, are superimposed on the pressure–time signal after about 130 s. While these complicate interpretation, the elevated pressure for the two minutes of central uplift formation and collapse is a robust outcome of the model that is insensitive to the location of the domain boundary.

Data availability

All data generated or analysed during this study are included in this published Article. Other Expedition 364 data are available online (https://doi.org/10.14379/iodp.proc.364.2017).

38. Gulick, S. *et al.* in *Proceedings of the International Ocean Discovery Program Volume* 364 (eds Morgan, J. et al.) 1–46 (IODP, 2017).
39. Ortner, H., Reiter, F. & Acs, P. Easy handling of tectonic data: the programs Tectonics FP for Mac and Tectonics FP for Windows. *Comput. Geosci.* **28**, 1193–1200 (2002).
40. Collins, G. S. *et al.* Dynamic modeling suggests terrace zone asymmetry in the Chicxulub crater is caused by target heterogeneity. *Earth Planet. Sci. Lett.* **270**, 221–230 (2008).

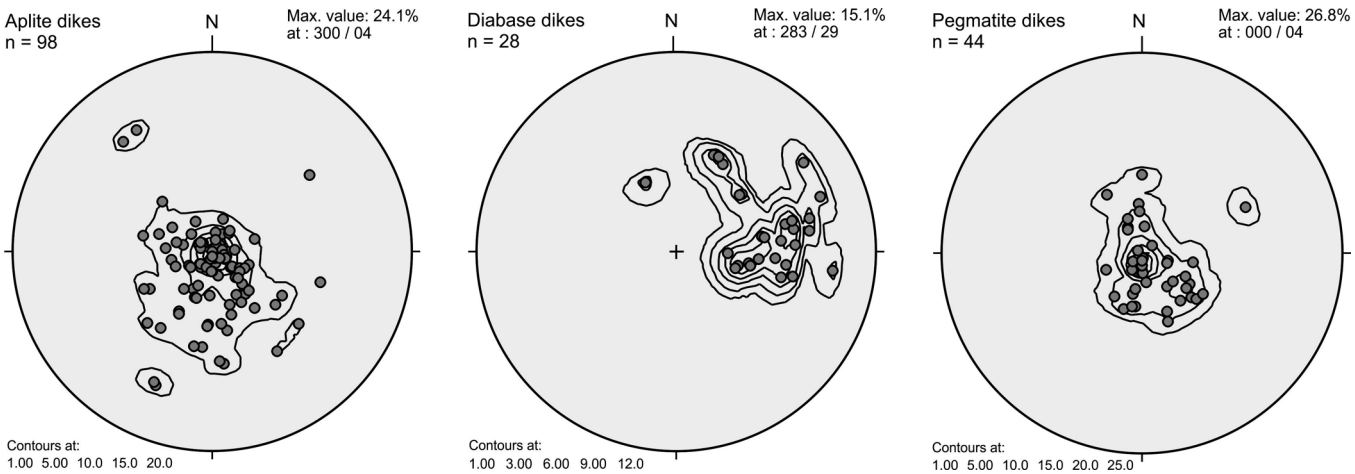

Extended Data Fig. 1 | Lower-hemisphere, equal-area diagrams showing poles to pre-impact aplite, diabase and pegmatite sheet intrusions. N, north. *n*, number of dykes.

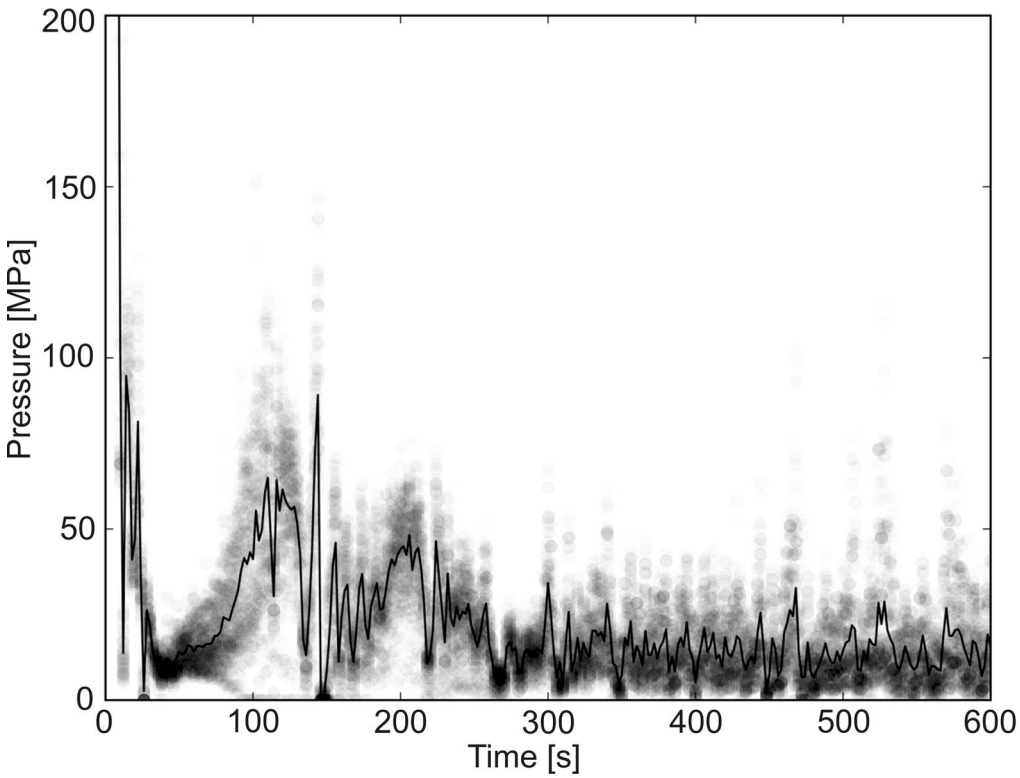

Extended Data Fig. 2 | Diagram showing pressure versus time as recorded by 100 Lagrangian tracer particles in the peak-ring rocks. (See Supplementary Video for location of tracer particles). Grey circles show the pressure of each tracer particle at time intervals of 2 s. The black solid line shows average pressure (all tracer particles). We note the elevated pressures between $T = 100$ s and $T = 250$ s during central uplift formation and collapse.